

# Progressive- $X^+$ : Clustering in the Consensus Space

Daniel Barath<sup>1</sup>, Denys Rozumny<sup>1,3</sup>, Ivan Eichhardt, Levente Hajder<sup>2</sup> and Jiri Matas<sup>3</sup>

<sup>1</sup> Department of Computer Science, ETH Zurich, <sup>2</sup> Eotvos Lorand University, Budapest

<sup>3</sup> Visual Recognition Group, Czech Technical University in Prague,

## Abstract

We propose *Progressive- $X^+$* , a new algorithm for finding an unknown number of geometric models, e.g., homographies. The problem is formalized as finding dominant model instances progressively without forming crisp point-to-model assignments. Dominant instances are found via RANSAC-like sampling and a consolidation process driven by a model quality function considering previously proposed instances. New ones are found by clustering in the consensus space. This new formulation leads to a simple iterative algorithm with state-of-the-art accuracy while running in real-time on a number of vision problems. Also, we propose a sampler reflecting the fact that real-world data tend to form spatially coherent structures. The sampler returns connected components in a progressively growing neighborhood-graph. We present a number of applications where the use of multiple geometric models improves accuracy. These include using multiple homographies to estimate relative poses for global SfM; pose estimation from generalized homographies; and trajectory estimation of fast-moving objects.

## 1. Introduction

Robust multi-instance model fitting is the problem of interpreting a set of data points as a mixture of noisy observations stemming from multiple instances of geometric models. Examples for such a problem are the estimation of plane-to-plane correspondences (i.e., homography matrices) in two images, and the retrieval of rigid motions in a dynamic scene captured by a moving camera. In the state-of-the-art algorithms, finding an unknown number of model instances is achieved by clustering the data points into disjoint sets, each representing a particular model instance. Robustness is achieved by considering an outlier model.

Multi-instance model fitting has been studied since the early sixties. The Hough-transform [24, 25] perhaps is the first popular method for finding multiple instances of a single class [20, 38, 45, 66]. The RANSAC [18] algorithm was as well extended to deal with finding multiple instances. Se-

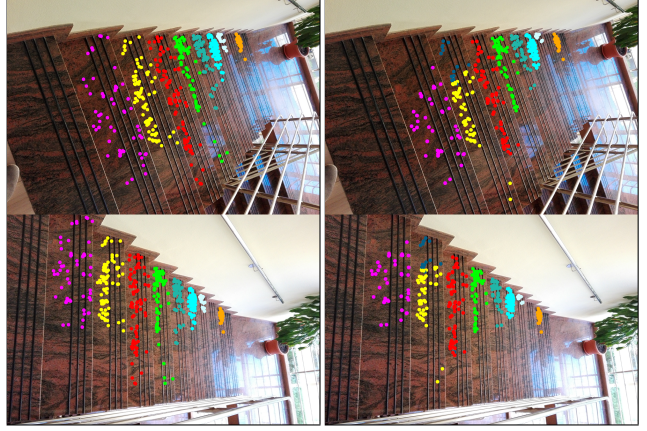


Figure 1: Multi-homography fitting with the proposed *Progressive- $X^+$*  in 0.04 secs (left), and with *Progressive-X* [5] in 1.48 secs (right). Outliers are not drawn.

quential RANSAC [59, 27] detects instances in a sequential manner by repeatedly running RANSAC to recover a single instance and, then, removing its inliers from the point set. The greedy approach that makes RANSAC a powerful tool for recovering a single instance becomes its drawback when estimating multiple ones. Points are assigned not to the best but to the first instance, typically the one with the largest support, for which they cannot be deemed outliers. MultiRANSAC [70] forms compound hypotheses about  $n$  instances. In each iteration, MultiRANSAC draws samples of size  $n$  times  $m$ , where  $m$  is the number of points required for estimating a model instance, e.g.,  $m = 4$  for homographies. Besides requiring the number  $n$  of the instances to be known a priori, the increased sample size affects the problem complexity and, thus, the processing time severely.

Modern approaches for multi-model fitting [65, 26, 41, 34, 35, 61, 36, 4, 1] follow a two-step procedure. First, they generate many instances by repeatedly selecting minimal point sets and fitting model instances. Second, a subset of the hypotheses is selected interpreting the input data points the most. This selection is done in various ways. For instance, a popular group of methods [26, 41, 4, 1] optimizes

point-to-model assignments by energy minimization using graph labeling techniques [9]. The energy originates from point-to-model residuals, label costs [16], and geometric priors [41] such as the spatial coherence of the data points. Another group of methods uses preference analysis based on the distribution of the residuals of data points [67, 34, 35, 36]. Also, there are techniques [61, 62, 68] approaching the problem as hyper-graph partitioning where the instances are represented by vertices, and the points by hyper-edges.

The recently published Progressive-X [5] discussed that the first, instance generation, step of the mentioned methods leads to a number of issues, *e.g.*, the instances are generated blindly, having no information about the data at hand. This approach severely restricts the out-of-the-box applicability of such techniques since the user either has to consider the worst-case scenario and, thus, generate an unnecessarily high number of instances; or requires some rule of thumb, *e.g.*, to generate twice the point number hypotheses that provides no guarantees of finding the sought instances. Prog-X [5] approaches the problem via interleaving the model proposal and optimization steps. The idea was recently combined with deep-learning-based sampling in [28] which was shown to further improve the accuracy.

A common point of the state-of-the-art algorithms is formalizing the multi-model fitting problem as finding disjoint sets of data points each representing a model instance. There are two main practical issues with this assumption. *First*, in some cases, a point belongs to multiple instances and this assumption renders the problem *unsolvable*, see the left image of Fig. 2. Also, the point-to-model assignment is often unclear even if it is done by a human, especially, for points around the intersection of instances, see the right two plots of Fig. 2 for examples. The *second* issue stems from the recovery of disjoint point sets that usually requires a rather complex procedure, *e.g.* labeling via energy minimization, that affects the run-time severely.

The *main* contribution of this paper is a fundamentally new problem formulation that does not require forming crisp point-to-model assignments, *i.e.*, a point can be assigned to multiple instances. This property allows the proposed Progressive-X<sup>+</sup> to be a simple iterative algorithm and, yet, to obtain results superior to the state-of-the-art both in terms of accuracy and run-time, being *real-time* on a number of problems, see Fig. 1. Also, this assumption relaxes the greedy nature of sequential algorithms as the ordering in which the instances are proposed becomes unimportant. As the *second* contribution, we propose a new sampler designed specifically for multi-instance model fitting. The sampler considers that real-world data tend to form spatially coherent structures. It returns the connected components in a gradually densified neighborhood-graph. As the *third* contribution, we discuss ways of exploiting multiple instances in popular applications – Structure-from-Motion,

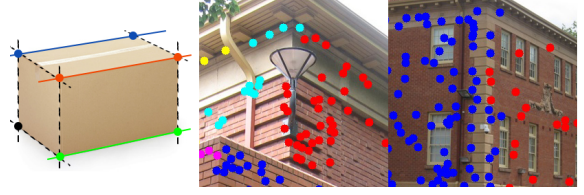


Figure 2: **Left:** A case when assigning points to a single line (by color) prevents finding all 9 instances. Dashed black lines are not recovered. When fitting planes to 4 out of the 7 points, only a single plane can be found. **Middle, Right:** Examples where the point-to-model assignment fails around the intersection of model instances, *e.g.*, planes.

pose estimation for generalized and pin-hole cameras, and trajectory estimation of fast-moving objects. By considering multiple models, the accuracy is increased in almost all cases on several publicly available real-world datasets.

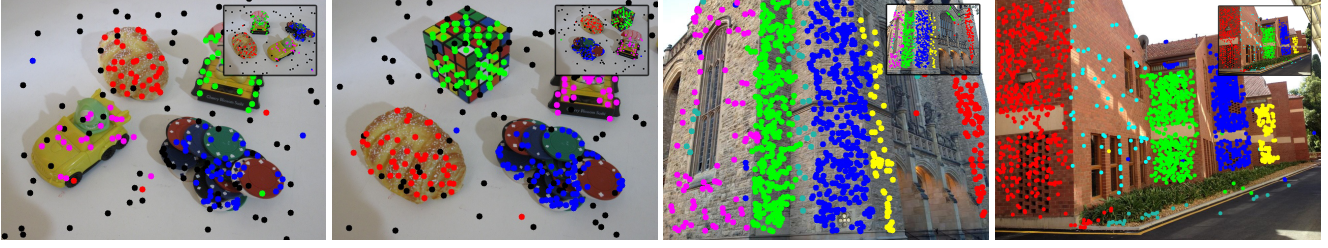
## 2. Progressive-X<sup>+</sup> Algorithm

We propose a new algorithm for robust multi-instance model fitting that combines the advantages of state-of-the-art algorithms and, also, follows a new formulation that does not require crisp point-to-model assignments for finding the dominant model instances.

### 2.1. Idea and Schematic Algorithm

The Progressive-X<sup>+</sup> algorithm is motivated by two observations about the nature of multi-model fitting problems. First, even though all state-of-the-art algorithms [26, 41, 36, 4, 1, 62, 5, 28] formalize the problem as a clustering where a set of data points (cluster) represents a model instance, this assumption is incorrect in a number of real-world scenes. Moreover, one of the primary reasons of multi-model fitting algorithms often being fairly slow stems from the optimization techniques, *e.g.*  $\alpha$ -expansion in PEARL [26], needed to solve the point-to-model assignment problem.

Our second observation is that multi-model fitting can usually be rephrased as the problem of finding multiple *dominant* instances that are reasonably *different*. Ideally, a *dominant* instance is one that represents a real structure. Since this is not an algorithmically measurable property, we define being dominant as having a reasonably large support not shared with other dominant instances. We consider instances *different* if they are “far” on the model manifold as proposed in [4]. This simple formulation allows us to avoid applying complex procedures finessing to interpret point-point, model-model, and point-model interactions. Also, it further relaxes the greedy nature of the progressive model proposal strategy introduced in [5] that enables to discover the data gradually. The pseudo-code of formalizing the multi-model problem as finding different



(a)  $ME_{\min}$ : 5.9%,  $ME_{\max}$ : 5.9% (b)  $ME_{\min}$ : 3.4%,  $ME_{\max}$ : 3.4% (c)  $ME_{\min}$ : 6.1%,  $ME_{\max}$ : 9.4% (d)  $ME_{\min}$ : 2.2%,  $ME_{\max}$ : 4.1%

Figure 3: Image pairs used for multiple two-view motion and homography estimation, and point-to-model assignments (by color) determined by assigning each point to one of the instances returned by Progressive- $X^+$  with the minimum point-to-model residual. Black points are outliers. For each image, the highest ( $ME_{\max}$ ) and lowest ( $ME_{\min}$ ) misclassification errors in five runs are reported. The least accurate results are shown. In (a–b), the worst and best results are identical. In (c–d), the difference is negligible. Progressive- $X^+$  finds all sought instances, the error originates from points assigned to the wrong instance. The selected scenes are the ones with the most ground truth instances to be found in the AdelaideRMF [65] dataset.

dominant model instances is as follows:

**Input:**  $\mathcal{P}$  – data points

**Output:**  $\mathcal{I}$  – model instances

$\mathcal{I} \leftarrow \emptyset$

**while**  $\neg \text{Terminate}()$  **do**

$\mathcal{I} \leftarrow \mathcal{I} \cup \text{FindDominantInstances}(\mathcal{P})$

**while**  $\neg \text{Convergence}()$  **do**

$\mathcal{I} \leftarrow \text{SelectDifferentInstances}(\mathcal{I})$

$\mathcal{I} \leftarrow \text{ImproveParameters}(\mathcal{I}, \mathcal{P})$

## 2.2. Finding Dominant Model Instances

Given a set of data points  $\mathcal{P}$  and a set of dominant model instances  $\mathcal{I}$  proposed in earlier iterations, the objective is to find a new dominant model instance  $h$  which should be included in  $\mathcal{I}$ . In the first iteration,  $\mathcal{I} = \emptyset$ .

To do so, we start similarly as RANSAC by first drawing a random sample  $\mathcal{S}$  of data points. This is done by a state-of-the-art sampler, *e.g.*, PROSAC [12] or P-NAPSAC [7]. Model instance  $h$  is estimated from sample  $\mathcal{S}$ . In order to decide about  $h$  being dominant or not, we define model quality function  $Q : \mathbb{R}^d \times \mathcal{P}^* \times \mathbb{R} \rightarrow \mathbb{R}$  similarly as [5] to be calculated from the inliers of  $h$  not shared with other instances in  $\mathcal{I}$ , where  $\mathcal{P}^*$  is the power set of  $\mathcal{P}$ . Considering the RANSAC-like inlier counting, the implied quality is

$$Q_{\text{RSC}}(h, \mathcal{P}, \epsilon) = \sum_{\mathbf{p} \in \mathcal{P}} [\phi(h, \mathbf{p}) < \epsilon \wedge \phi(\mathcal{I}, \mathbf{p}) \geq \epsilon],$$

where  $\epsilon \in \mathbb{R}$  is the inlier-outlier threshold and  $\phi(\mathcal{I}, \mathbf{p}) = \min_{h \in \mathcal{I}} \phi(h, \mathbf{p})$  is the minimal point-to-model residual of point  $\mathbf{p}$  given the kept set of dominant model instances  $\mathcal{I}$ . In order to use the recent advances of RANSAC, *e.g.*, the loss function of MAGSAC++ [7] the currently most accurate method according to a recent survey [33],  $Q_{\text{RSC}}$  is reformulated considering a continuous loss function  $f$ . For practical considerations, we consider losses returning a value

in-between 0 and 1. The quality function that  $f$  implies is

$$Q_f(h, \mathcal{P}, \epsilon) = |\mathcal{P}| - \sum_{\mathbf{p} \in \mathcal{P}} \max(f(h, \mathbf{p}), 1 - f(\mathcal{I}, \mathbf{p})),$$

where  $f(\mathcal{I}, \mathbf{p}) = \min_{h \in \mathcal{I}} f(h, \mathbf{p})$  is the minimum loss of point  $\mathbf{p}$  given the set of kept instances  $\mathcal{I}$ . It can be easily seen that this quality function returns high score to those instances which do not share inliers with any of the instances from  $\mathcal{I}$ . Otherwise, the quality is reduced according to the number and residuals of the inliers shared.

To determine whether instance  $h$  is dominant, we introduce parameter  $q_{\min}$ , and all model instances are considered dominant where  $Q_f(h, \mathcal{P}, \epsilon) \geq q_{\min}$ . This constraint can be interpreted as a lower bound for the number of perfectly fitting data points which are not shared with any of the instances from the maintained set in  $\mathcal{I}$ .

In the actual algorithm, we used the MAGSAC++ quality function [7] and, thus,  $\epsilon$  is not an inlier-outlier threshold but its loose upper bound. We also tested Tukey-bisquare, Huber, redescending Huber, and MSAC losses. While Tukey-bisquare and MSAC lead to reasonably accurate solutions, MAGSAC++ leads to the most accurate results on all tested problems. The setting of  $q_{\min}$  is easy,  $q_{\min} = 20$  works for most of the problems which we tested. Also, instead of inserting a single instance in  $\mathcal{I}$ , we add multiple ones in each iteration. In all our tests, adding 10 instances worked well.

## 2.3. Clustering in the Consensus Space

The next step of the algorithm, after a set  $\mathcal{I}$  of dominant model instances have been found, is to select a subset of  $\mathcal{I}$  consisting of instances that represent different model instances and not the noisy observations of the same one. We define a model-to-model residual function  $\psi : \mathbb{R}^d \times \mathbb{R}^d \rightarrow \mathbb{R}$  measuring the distance of two model instances.

**Model-to-model residual.** Defining a reasonable model-to-model residual function is a challenging problem. In the





Figure 4: Examples where converting homographies to points and back is not robust. **Left:** top two corners are mapped to the same location. Thus, three matches remain for the homography recalculation. **Right:** the ordering of the points along the convex hull changes and the recovered homography will be incorrect when the plane flips.

Multi-X algorithm [4], it was proposed to convert the model instances to point sets. The distance of two instances is the Hausdorff distance [44] of the point sets representing them. This solution is however a challenging task since the conversion of geometric models to point sets in a robust manner is unclear in most of the cases. Even for homographies, there is a number of cases when this approach simply does not work, see Fig. 4 for examples. Instead, we follow the strategy proposed in the T-Linkage algorithm [34] to measure the model-to-model residual as the Tanimoto distance of the preference vectors [56] as follows:

$$f_T(v_a, v_b) = \frac{\langle v_a, v_b \rangle}{\|v_a\|^2 + \|v_b\|^2 - \langle v_a, v_b \rangle}.$$

The preference vector of a model instance  $h$  is  $v \in [0, 1]^n$ , where  $n$  is the number of input data points. Its  $i$ th coordinate is calculated as  $v_i = 1 - f(h, \mathbf{p}_i)$ , where  $f$  is the same loss function as what is used in the previous section and  $\mathbf{p}_i$  is the  $i$ th point from  $\mathcal{I}$ . Briefly,  $v_i$  is zero if the point-to-model residual is greater than the inlier-outlier threshold. Otherwise, it is from interval  $(0, 1]$ . In this case, the Tanimoto distance measures the overlap of the inlier sets of two model instances where the inlier assignment is done in a smooth manner. We will call the domain of preference vectors *consensus space* in the rest of the paper. It is important to note that, while the Tanimoto distance is not a proper distance metric over general vector spaces, it becomes one when having only positive numbers or zeros in the vectors [32]. This property holds in our case.

**Clustering.** We formulate the problem of selecting different model instances as finding similar ones in  $\mathcal{I}$  which are then replaced by a single instance. A straightforward strategy for finding similar instances is to find clusters in the consensus space defined over the preference vectors.

In general, this clustering takes place in an extremely large dimensional space, with as many dimensions as many input data points. In this particular setup however, we never have more than a few tens of instances to be clustered thanks

to the progressive proposal strategy adapted from [5]. This means that the clustering is done on a few high-dimensional vectors that is very efficient with most of the clustering algorithms. Even if there are millions of points in the scene, a single model instance rarely has an extreme number of inliers and, thus, the indices of the non-zero elements in  $v$  can be stored, making the distance calculation more efficient. In extreme cases, the min hash algorithm [10] can approximately find the inlier overlap in constant time.

After obtaining a set of instance clusters, the next step is to replace the instances in each cluster with a single one. Even though it would be a straightforward way to use the density modes, *e.g.* as in [15], it requires doing operations with the preference vectors, *e.g.* averaging. However, such operations are undefined in the consensus space – the average of two vectors is not necessarily the preference vector of the average instance. Thus, we replace each cluster with one of its elements that has the highest quality  $Q_f$  and, thus, is the most likely to represent the sought model parameters.

In the actual algorithm, we used the DBSCAN [17, 52] density-based clustering that runs swiftly on our problem and returns accurate solutions. DBSCAN requires two parameters, *i.e.*, the minimum size  $c_{\min}$  of a cluster to be kept and a threshold  $\epsilon_T$  to decide if two model instances are neighbors in the consensus space. The minimum size  $c_{\min} = 1$  since single-element clusters also contain dominant model instances and, thus, should be kept. The setting of threshold  $\epsilon_T$  is intuitive and easy. In most of our experiments, we used  $\epsilon_T = 0.2$ , considering two instances neighbors if their Tanimoto distance is smaller than 0.2. This can roughly be interpreted as considering two model instances similar if more than 20% of their inliers are shared.

## 2.4. Improving Instance Parameters

In order to improve the parameters of the instances kept by the clustering algorithm, we apply an iteratively re-weighted least-squares approach starting from the initial instance parameters. We use the robust MAGSAC++ weights.

The model optimization and clustering are applied repeatedly since during the optimization step two instances might become similar and, thus, should be put in the same cluster. This iteration stops when only one-element clusters are returned by the applied clustering algorithm.

## 2.5. Termination Criterion

To decide when the algorithm should terminate, we used the criterion proposed in [5] that is as follows:

$$n_i = (|\mathcal{P}| - |\mathcal{I}|) \sqrt[m]{1 - \frac{k}{\sqrt{1 - \mu}}} \leq m + 1, \quad (1)$$

where  $\mu$  is the required confidence in the results typically set to 0.95 or 0.99;  $k$  is the number of iterations;  $m$  is the size of the minimal sample;  $n_i$  and  $|\mathcal{P}|$  are the number of



---

**Algorithm 1** Connected Component Sampler: the next  $\mathcal{S}$ .

---

**Input:**  $r, r_{\min}, r_{\max}, n_{\text{steps}}$  – current, min., max. neighborhood radius and partition number;  $\mathcal{P}$  – data points;  $\mathcal{A}$  – neighborhood-graph;  $m$  – sample size

**Output:**  $\mathcal{S}$  – sample

```
if  $\neg \text{Initialized}(\mathcal{A})$  then ▷ Run only once
   $\mathcal{A} \leftarrow \text{BuildNeighborhood}(\mathcal{P}, r_{\max})$  ▷ Radius is  $r_{\max}$ 
   $r \leftarrow r_{\min}$  ▷ The max. radius in  $\mathcal{A}$  for the next step
   $\mathcal{C} \leftarrow \text{GetConnectedComponents}(\mathcal{A}, r)$ 

while  $\text{Empty}(\mathcal{C}) \wedge r \leq r_{\max}$  do
   $r \leftarrow r + (r_{\max} - r_{\min}) / n_{\text{steps}}$ 
   $\mathcal{C} \leftarrow \text{GetConnectedComponents}(\mathcal{A}, r)$ 

 $\mathcal{S} \leftarrow \emptyset$ 
if  $\neg \text{Empty}(\mathcal{C})$  then
  repeat ▷ Get the next largest dominant instance
     $\mathcal{S} \leftarrow \text{GetLargest}(\mathcal{C}), \mathcal{C} \leftarrow \mathcal{C} \setminus \text{GetLargest}(\mathcal{C})$ 
  until  $|\mathcal{S}| \geq m \vee \text{Empty}(\mathcal{C})$ 

if  $|\mathcal{S}| < m$  then
   $\mathcal{S} \leftarrow \text{PROSAC}(\mathcal{P}, m)$ 
```

---

inliers and points; and  $|T|$  is the cardinality of the united inlier sets of the kept model instances. This criterion is triggered if the probability of having an unseen model with at least  $m + 1$  inliers is smaller than  $1 - \mu$ . Since we have a criterion for an instance being dominant, the upper bound  $m + 1$  for  $n_i$  can be replaced by  $q_{\min}$  to terminate when the probability of finding a dominant instance falls below  $1 - \mu$ .

### 3. Connected Component Sampling

There have been a number of algorithms proposed, *e.g.* PROSAC [12], P-NAPSAC [7], to find samples that consist of data points stemming from the same model instance early. When fitting multiple instances to real-world data, it usually is a reasonable assumption that the points form spatially coherent structures [39, 26, 3, 7]. We propose a deterministic sampling that returns the connected components in a progressively densified neighborhood-graph as samples. The algorithm is shown in Alg. 1.

The user-defined parameters are the minimum ( $r_{\min}$ ) and maximum ( $r_{\max}$ ) neighborhood radii and the number of steps when densifying the graph ( $n_{\text{steps}}$ ). As initialization, the method first builds neighborhood-graph  $\mathcal{A}$  using the maximum radius. Then the connected components are selected from a sub-graph of  $\mathcal{A}$  where all edges are removed that are larger than the current radius  $r$ . This is done to avoid building  $\mathcal{A}$  multiple times. The algorithm returns the largest connected component that has at least  $m$  points. If there is no such component, it increases the neighborhood size by changing  $r$ . Note that the returned sample  $\mathcal{S}$  is not necessarily a minimal sample. If  $r$  exceeds  $r_{\max}$ , there are no reasonable structures and, thus, it starts sampling from

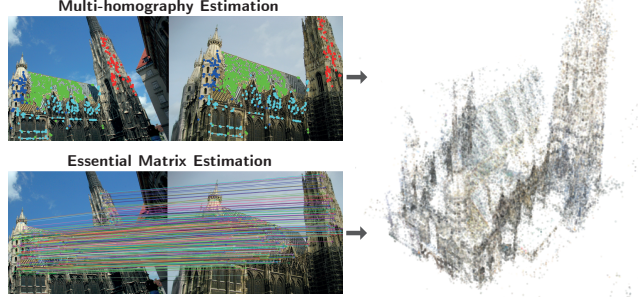


Figure 5: Multiple homographies contribute to the accurate reconstruction of Vienna Cathedral by [55]. The rotation and position errors are decreased, respectively, by  $9.8^\circ$  and 5.0 m on average compared to using  $\mathbf{E}$  matrices only.

all data points in a global manner by the PROSAC sampler. Also note that while PROSAC is a safe-guard for cases where the data is not spatially coherent, it was *never* actually required in our experiments.

## 4. Experimental Results

**Implementation Details.** The Progressive- $X^+$  algorithm is implemented in C++ using the Eigen library and the solver implementation from the GC-RANSAC [3] repository. We combine the algorithm with a number of components from USAC [43]. The included components are the following.

*Sample degeneracy.* The degeneracy tests of minimal samples are for rejecting clearly bad samples to avoid the sometimes expensive model estimation. For homographies, samples consisting of collinear points are rejected.

*Sample cheirality.* The test is for rejecting samples based on the assumption that both of the cameras observing a 3D surface must be on its same side. For homography fitting, we check whether the ordering of the four point correspondences – along their convex hulls – in both images are the same. If not, the sample is rejected.

*Model degeneracy.* The purpose of this test is to reject models early to avoid verifying them unnecessarily. For fundamental matrices (*i.e.*, two-view motion), DEGENSAC [14] is applied to determine whether the epipolar geometry is affected by a dominant plane.

*Model cheirality.* The test is for rejecting models considering that the cameras must be on the same side of the observed surface. For fundamental and essential matrix estimation, we apply the oriented epipolar constraint [13].

*Parameters.* Model-to-model threshold  $\epsilon_T = 0.2$ ; minimum quality  $q_{\min} = 20$ ; confidence  $\mu = 0.99$ ; radii  $r_{\min} = 20$ ,  $r_{\max} = 200$ ,  $r_{\text{steps}} = 5$ ; 10 dominant models are added in each iteration. For point correspondences, the neighborhood is built on the joint 4D coordinate space.

## 4.1. Traditional Problems

To evaluate the proposed method on real-world problems, we downloaded a number of publicly available datasets for homography, two-view motion, and motion fitting. The error is the misclassification error (ME), *i.e.*, the ratio of points assigned to the wrong cluster. Progressive- $X^+$  is designed to avoid assigning each data point to a single instance. Thus, we assigned each point to the model with the smallest residual. The results of the compared methods are copied from [5, 28], where they were carefully tuned to achieve their best results with fixed parameters.

In order to test the proposed connected component-based sampler, we applied Progressive- $X^+$  with P-NAPSAC [7] and the proposed Connected Component Sampler. We chose P-NAPSAC as a competitor, since it has a similar procedure, finding local structures by randomly sampling from gradually growing neighborhoods. The major difference between them is that P-NAPSAC is randomized and returns minimal samples, while the proposed Connected Component Sampler is deterministic and proposes larger-than-minimal samples as well.

Example results of multi-homography and two-view motion fitting are in Fig. 3. We chose the scenes from the AdelaideRMF [65] dataset having the most ground truth instances to be found. Color denotes the point-to-model assignment done by assigning each point to the instance, outputted by Progressive- $X^+$ , with the smallest residual.

**Two-view motion** fitting is evaluated on the AdelaideRMF motion dataset consisting of 21 image pairs of different sizes and correspondences manually assigned to two-view motion clusters. In this case, multiple fundamental matrices are to be found. For the proposal step in each iteration, we used the seven-point algorithm [22]. In the IRLS fitting, we applied the normalized eight-point technique [21].

The avg. errors over five runs and their standard deviations are shown in the left block of Table 1. Progressive- $X^+$ , with both tested samplers, leads to state-of-the-art accuracy. The proposed Connected Components Sampler (CC) improves both the accuracy and processing time. Progressive- $X^+$  with CC is twice as accurate as the second best method (Prog-X) while being two orders-of-magnitude faster than the second fastest method (Multi-X). Progressive- $X^+$  runs in *real-time* on these scenes.

**Homography** fitting is evaluated on the AdelaideRMF homography dataset [65] used in most recent publications. AdelaideRMF consists of 19 image pairs of different resolutions with ground truth point correspondences assigned manually to homographies. In these tests, we also included the errors of CONSAC [28]. Since the processing times are not reported in [28], we re-ran the algorithm both on GPU and CPU and calculated the average run-times.

We used the normalized four-point algorithm both in the proposal and IRLS steps. The results are shown in the mid-

dle block of Table 1. Similarly as for two-view motion fitting, Progressive- $X^+$  is almost twice as accurate as the second best method (*i.e.*, CONSAC) and it is significantly faster than all of the compared algorithms. Progressive- $X^+$  leads to the most accurate solutions while being the fastest. In this case, P-NAPSAC sampler leads to the best results.

**Motion** segmentation is tested on the 155 videos of the Hopkins dataset [58]. The dataset consists of 155 sequences divided into three categories: checkerboard, traffic, and other sequences. The trajectories are inherently corrupted by noise, but no outliers are present. Motion segmentation in videos is the retrieval of sets of points undergoing rigid motions contained in a dynamic scene captured by a moving camera. It can be considered as a subspace segmentation under the assumption of affine cameras. For affine cameras, all feature trajectories associated with a single moving object lie in a 4D linear subspace in  $\mathbb{R}^{2F}$ , where  $F$  is the number of frames [58].

The results are shown in the right block of Table 1. Progressive- $X^+$  leads to the lowest errors. While it is the second fastest algorithm, it still runs in *real-time*. We did not use the Connected Component Sampler since building a neighborhood-graph on point trajectories is slow and setting the neighborhood radius parameter is unclear.

## 4.2. Application: Relative Pose Estimation

In this section, we focus on improving relative pose estimation by exploiting multiple homographies. Pose estimation is a fundamental problem in a number of popular methods, *e.g.*, in Structure-from-Motion (SfM) algorithms. While the usual procedure to estimate a relative pose uses epipolar geometry, it is well-known that the pose can also be obtained from a homography if the cameras are calibrated. However, in most pipelines, homographies are used only if the scene is degenerate for fundamental matrix estimation, *e.g.*, a single plane dominates the scene [14] or the camera undergoes purely rotational motion. In this section, we aim to explore ways of exploiting multiple homographies to improve the relative pose accuracy. See Fig. 5 for an example.

We downloaded the 1DSfM dataset [63] and applied COLMAP [51] to obtain a reconstruction that can be used as ground truth. Note that the 1DSfM dataset provides a ground truth, however, it was created by the Bundler algorithm [53] that is more than 10 years old. We use the following approach in order to find potentially matching image pairs. First, we extract GeM [42] descriptors with ResNet-50 [23] CNN, pre-trained on GLD-v1 dataset [40]. Then we calculate the inner-product similarity between the descriptors, resulting in an  $n \times n$  similarity matrix. In the experiments, we use only the image pairs with similarity higher than 0.4 [6]. Finally, we estimated multiple homographies for all considered image pairs, 434 587 in total.

We tested the following approaches to recover the rela-

tive pose from multiple homographies.

1. Estimating the essential matrix [54] from all point correspondences which were inliers of a returned homography.
2. Decomposing each homography and, also, the essential matrix to pose and running pose averaging by [11, 64].
3. Decomposing each homography [37] and, also, the essential matrix to pose and selecting the one which has the most inliers determined by thresholding the re-projection error. The translation is then re-estimated by solving equation  $\mathbf{p}_2^T [\mathbf{t}]_{\times} \mathbf{R} \mathbf{p}_1 = 0$  with known rotation  $\mathbf{R}$ , where  $[\mathbf{t}]_{\times}$  is the cross-product matrix of translation  $\mathbf{t}$  and  $[\mathbf{t}]_{\times} \mathbf{R}$  is the essential matrix. Details are in the supplementary material.

The results are reported in the top of Table 5. Results when using the proposed connected component sampler (CC) are also shown. To measure the error in the rotation, we calculate the angular difference between the ground truth  $\hat{\mathbf{R}}$  and estimated  $\mathbf{R}$  ones as  $\epsilon_{\mathbf{R}} = \cos^{-1}((\text{tr}(\mathbf{R}\hat{\mathbf{R}}^T) - 1)/2)$ . Since the translation is up to scale, the error is the angular difference  $\epsilon_t$  of the ground truth and estimated translations. The average rotation and translation errors are improved by, respectively, 1.27 and 0.34 degrees compared to  $\mathbf{E}$  estimation. Due to Progressive- $\mathbf{X}^+$  being extremely fast, the computational overhead is merely a few *ms* per image pair.

We applied the global SfM implemented in the Theia library [55] initialized with the pose graph estimated in the proposed way and, also, with the pose graph estimated using only essential matrices. The accuracy of the reconstruction is reported in the bottom part of Table 5. We report the average rotation (avg.  $\epsilon_{\mathbf{R}}$ , in degrees) and position errors (avg.  $\epsilon_p$ , in meters) and, also, the median errors averaged over the scenes. The proposed algorithm with the connected components sampler *significantly* reduces both the rotation and position errors of the reconstruction.

### 4.3. Application: Fast-moving Object Detection

In this section, we estimate the trajectories of objects that are significantly blurred by their motion. As defined in [47], an image  $I$  of such blurred object is formed as a composition of the blurred object appearance and the background

$$I = H * F + (1 - H * M) B, \quad (2)$$

where the sharp object appearance  $F$  with mask  $M$  encodes the object, blur kernel  $H$  encodes the trajectory, and  $B$  represents the background. Input image  $I$  and background  $B$  are assumed to be known. The unknowns in (2) are estimated either by alternating energy minimization with additional priors [30, 48, 46, 31, 29], or more recently by learning from synthetic data [50, 49].

The formation model in (2) encodes the trajectory by the blur kernel. However, there are no guarantees that the blur kernel corresponds to a physically plausible trajectory, which is assumed to be piece-wise linear due to bounces. Blur kernels also contain other responses due to

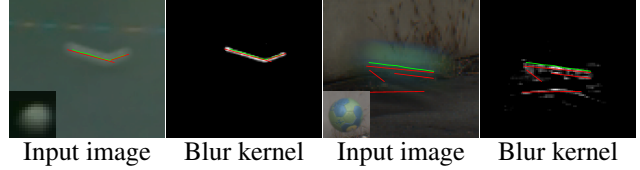


Figure 6: Multiple line segment fitting for trajectory estimation of fast-moving objects. Estimated line segments are in red, the ground truth is in green. Sharp object appearance is overlaid in the bottom left corner of the input image.

other moving objects in the scene. In the extreme case, if two fast-moving objects intersect or fly close to each other, the blur kernel will contain multiple responses corresponding to each motion separately. In practice, the estimated blur kernels are noisy, with many outliers, and contain artifacts due to shadows, low contrast, and discretization. Motion blur priors [60] have been proposed to reduce these issues, but extracting the final continuous trajectory is still a challenging multi-instance model fitting task (see Fig. 6).

Recent methods [30, 48] address this task by employing Sequential RANSAC [59, 27] on the thresholded blur kernels. For the experiments, we extract blur kernels using the TbD method [30] from all sequences in the TbD [30] and TbD-3D [48] datasets. The TbD dataset is simpler since it contains mostly uniformly colored objects moving in the plane parallel to the camera plane. The TbD-3D dataset is more challenging with highly textured objects that are rotating and moving in 3D. The ground truth sub-frame object location is given from a high-speed camera. We estimate multiple line segments in each blur kernel and measure the average  $L_2$  distance of each ground truth location to the closest fitted line segment. Table 4 shows the average error, its standard deviation, and average run-time for a wide range of state-of-the-art methods. We used the implementations provided by the authors. The proposed Prog- $\mathbf{X}^+$  method outperforms all compared algorithms both in terms of accuracy and processing time, running in *real-time*.

### 4.4. Pose from Generalized Camera

To further test the pose selection technique from multiple homographies and an essential matrix, as proposed in Section 4.2, we downloaded the KITTI odometry dataset [19], where each frame consists of the images of two cameras. We considered the two cameras as a generalized one and estimated the pose between this camera and the left image of the next frame. We used the generalized essential matrix [69] ( $\mathbf{E4+2}$ ) and homography [8] ( $\mathbf{H3+2}$ ) solvers. For finding a single  $\mathbf{E4+2}$  or  $\mathbf{H3+2}$ , we used GC-RANSAC [3]. The methods were tested on a total of 23 190 frame pairs.

The results are reported in Table 3. The proposed technique ( $\mathbf{E} + \text{mult. } \mathbf{Hs}$ ), selecting the best pose from the set



		Two-view motions			Homographies			Motions		
		18 scenes			19 scenes			155 scenes		
	$ Z $ needed	avg.	std.	time	avg.	std.	time	avg.	std.	time
<b>Prog-X<sup>+</sup></b>	no	8.14	6.31	0.05	<b>3.10</b>	<b>3.45</b>	<b>0.11</b>	<b>4.41</b>	<b>6.34</b>	0.04
<b>Prog-X<sup>+</sup> (CC)</b>	no	<b>4.91</b>	<b>4.26</b>	<b>0.02</b>	5.73	6.52	<b>0.11</b>	—	—	—
Prog-X [5]	no	10.73	8.73	14.38	6.86	5.91	1.03	8.41	10.29	<b>0.02</b>
Multi-X [4]	no	17.13	12.23	1.52	8.71	8.13	0.27	12.96	19.60	0.95
PEARL [26]	no	29.54	14.80	4.94	15.14	6.75	2.61	14.25	23.23	3.30
RPA [35]	yes	17.11	11.08	10.24	23.54	13.42	622.87	9.16	11.26	4.92
RansaCov [36]	yes	55.61	12.42	2.33	66.88	18.44	17.69	11.13	8.00	2.04
T-linkage [34]	no	46.67	15.60	2.69	54.79	22.17	57.84	27.24	15.57	0.95
CONSAC [28]	no	—	—	—	5.21	6.46	8.14 / 21.00	—	—	—

Table 1: Avg. misclassification errors (in %; 5 runs on each scene), their std. and the processing times (secs) on two-view motion and homography fitting on the AdelaideRMF dataset [65], and motion fitting on the Hopkins dataset [58]. All methods used fixed parameters. For CONSAC, we report the times of running it on GPU and CPU as well. The second column ( $|Z|$  needed) is “yes” for methods requiring the number of instances to fit. “CC” denotes the proposed sampler.

Relative Pose Estimation				
	avg. $\epsilon_R$	med. $\epsilon_R$	avg. $\epsilon_t$	med. $\epsilon_t$
<b>E</b> matrix	9.51	3.46	18.15	9.08
<b>E</b> from <b>Hs</b>	9.56	3.47	18.21	9.09
Pose averaging	8.71	3.69	34.34	25.27
Pose selection	8.33	3.34	17.84	8.92
Pose selection (CC)	<b>8.24</b>	<b>3.31</b>	<b>17.81</b>	<b>8.89</b>
Global SfM Results				
	avg. $\epsilon_R$	med. $\epsilon_R$	avg. $\epsilon_p$	med. $\epsilon_p$
<b>E</b> matrix	11.15	6.58	10.25	8.93
<b>E</b> + mult. <b>Hs</b>	7.93	6.21	10.52	4.60
<b>E</b> + mult. <b>Hs</b> (CC)	<b>5.56</b>	<b>5.61</b>	<b>9.57</b>	<b>3.99</b>

Table 2: **Relative Pose:** Relative rotation  $\epsilon_R$  and translation  $\epsilon_t$  errors (degrees) on 434 587 image pairs from the 1DSfM dataset obtained by **E** matrix estimation; calculating **E** from the inliers of homographies (**E** from **Hs**); pose averaging on the poses decomposed from **E** and multiple **Hs** (Pose averaging); and selecting the pose with the most inliers from the decomposed ones (Pose selection) with the proposed sampler (CC). **Global SfM:** Rotation and position errors (meters) of the global SfM from [55] when initialized with a pose-graph estimated from **E** matrices, and via pose selection from multiple homographies and **E**.

decomposed from an essential matrix and multiple homographies, leads to the most accurate results in terms of average rotation and position errors. Its median rotation error is similar to **H3+2**. Its median position error is the lowest.

## 5. Conclusion

We proposed a new multi-instance model fitting algorithm, Progressive-X<sup>+</sup>, that is a simple iteration of instance proposal, clustering in the consensus space, and parameter re-estimation. Due to not forming crisp point-to-model assignments, the method runs in *real-time* on a number of vi-

	avg. $\epsilon_R$	med. $\epsilon_R$	avg. $\epsilon_p$	med. $\epsilon_p$
<b>E4+2</b>	1.19	0.50	0.033	0.025
<b>H3+2</b>	0.45	<b>0.24</b>	0.103	0.041
<b>E</b> + mult. <b>Hs</b>	<b>0.32</b>	0.26	<b>0.026</b>	<b>0.022</b>

Table 3: The avg. and med. rotation  $\epsilon_R$  (degrees) and position  $\epsilon_p$  (meters) errors on 23 190 image pairs from the KITTI dataset obtained by generalized essential matrix (**E4+2**) [69] and homography estimation [8] (**H3+2**); and by selecting the pose obtained from a generalized **E** matrix and a set of generalized homographies (**E** + mult. **Hs**).

Dataset:	Easy [30]			Challenging [48]		
Scene #:	322			470		
	avg.	std.	time	avg.	std.	time
<b>Prog-X<sup>+</sup></b>	<b>1.39</b>	6.73	<b>0.02</b>	<b>2.84</b>	<b>2.80</b>	<b>0.05</b>
Prog-X [5]	1.87	6.80	0.24	3.74	3.22	0.09
PEARL [26]	<b>1.39</b>	6.74	0.05	4.83	6.17	0.08
J-Linkage [57]	1.73	6.72	4.02	4.85	6.51	4.52
T-Linkage [34]	1.71	<b>6.71</b>	7.07	4.46	5.21	33.65
RPA [35]	2.74	7.77	7.66	5.19	4.47	21.79
RansaCov [36]	1.48	6.74	2.09	3.90	4.83	7.62
Seq. RANSAC	1.66	6.72	0.68	6.08	7.50	0.98

Table 4: The avg. and std. accuracy (in pixels) and run-time (in seconds) of multiple line segment detection for finding the trajectories of fast-moving objects on two datasets.

sion problems. It leads to results superior to the state-of-the-art in terms of accuracy on the traditionally used datasets. In addition, we demonstrated on a total of 458 569 images or images pairs that using multiple model instances, *e.g.* homographies or line segments, is beneficial for various popular vision applications, *e.g.*, Structure-from-Motion. The source code will be made public.

Global SfM Results				
Values in Table 2				
	avg. $\epsilon_R$	med. $\epsilon_R$	avg. $\epsilon_P$	med. $\epsilon_P$
<b>E</b> matrix	11.19	6.68	10.48	8.95
<b>E</b> + mult. <b>Hs</b>	7.35	6.21	10.53	4.55
<b>E</b> + mult. <b>Hs</b> (CC)	<b>5.91</b>	<b>5.64</b>	<b>9.66</b>	<b>3.98</b>
Correct Values				
	avg. $\epsilon_R$	med. $\epsilon_R$	avg. $\epsilon_P$	med. $\epsilon_P$
<b>E</b> matrix	11.15	6.58	10.25	8.93
<b>E</b> + mult. <b>Hs</b>	7.93	6.21	10.52	4.60
<b>E</b> + mult. <b>Hs</b> (CC)	<b>5.56</b>	<b>5.61</b>	<b>9.57</b>	<b>3.99</b>

Table 5: Rotation and position errors (meters) of the global SfM from [55] when initialized with a pose-graph estimated from **E** matrices, and via pose selection from multiple homographies and **E**. The top block shows the results reported in the main paper. The bottom shows the correct values. The difference is negligible. “CC” denotes the proposed sampler. Detailed results are in Table 6.

## 6. Supplementary Material

### 6.1. Structure-from-Motion Results

**Detailed results.** The results of the global SfM from [55] on each scene from the 1DSfM dataset are reported in Table 6. Note that we omitted the results on scenes Gendarmenmarkt and Union Square since [55] failed to reconstruct them with all tested pose-graph estimation techniques.

Additional visualizations are put in Figures 7 and 8, where the top rows show the results of [55] when initialized by a pose-graph estimated in the proposed way, exploiting an essential matrix and multiple homographies. The bottom rows show results when the pose-graph is estimated from essential matrices in the traditional way. Colored ellipses mutually highlight parts of the two reconstructions with noticeable differences. The traditional approach leads to reconstructions with fewer details and reduced precision compared to the proposed technique.

### 6.2. Translation from Known Rotation

In Section 4.2., we propose to estimate the relative pose from multiple homographies and the essential matrix by decomposing them and choosing the pose that leads to the most inliers when thresholding the re-projection error. We found that, while the estimated rotation matrix often is accurate, the translation can be improved by re-estimating it from the found inliers considering the known rotation.

In this section, we briefly describe the translation estimation procedure given a known rotation matrix. It is well-known [22] that the essential matrix is defined as

$$\mathbf{E} = [\mathbf{t}]_{\times} \mathbf{R},$$

where  $\mathbf{t} \in \mathbb{R}^3$  and  $\mathbf{R} \in \text{SO}(3)$  are, respectively, the transla-

tion vector and rotation matrix, and  $[\mathbf{t}]_{\times}$  is the cross-product matrix of  $\mathbf{t}$  as follows:

$$[\mathbf{t}]_{\times} = \begin{bmatrix} 0 & -t_z & t_y \\ t_z & 0 & -t_x \\ -t_y & t_x & 0 \end{bmatrix}.$$

Essential matrix **E** describes the relationship of a point correspondence in the images via the well-known epipolar constraint as follows:

$$\mathbf{p}_2^T \mathbf{E} \mathbf{p}_1 = 0,$$

where  $\mathbf{p}_1 = [u_1 \ v_1 \ w_1]^T$  and  $\mathbf{p}_2 = [u_2 \ v_2 \ w_2]^T$  are homogeneous points in the normalized image plane, *i.e.*, normalized by the intrinsic camera matrices. Considering **R** to be known, we are given the following constraint

$$\mathbf{p}_2^T [\mathbf{t}]_{\times} \mathbf{R} \mathbf{p}_1 = 0,$$

where the only unknowns are the three translation components  $\mathbf{t} = [t_x \ t_y \ t_z]^T$ . Multiplication  $\mathbf{R} \mathbf{p}_1$  can be pre-calculated as  $\mathbf{p}'_1 = \mathbf{R} \mathbf{p}_1$ . Formula  $\mathbf{p}_2^T [\mathbf{t}]_{\times} \mathbf{p}'_1$  leads to:

$$\begin{aligned} -u_2 t_z v'_1 + u_2 t_y w'_1 + v_2 t_z u'_1 - \\ v_2 t_x w'_1 - w_2 t_y u'_1 + w_2 t_x v'_1 &= 0. \end{aligned} \quad (3)$$

Eq. 3 is linear in the elements of the translation vector. Therefore, the equation can be reformulated as

$$\begin{bmatrix} v'_1 w_2 - w'_1 v_2 \\ u_2 w'_1 - w_2 u'_1 \\ v_2 u'_1 - u_2 v'_1 \end{bmatrix}^T \begin{bmatrix} t_x \\ t_y \\ t_z \end{bmatrix} = 0.$$

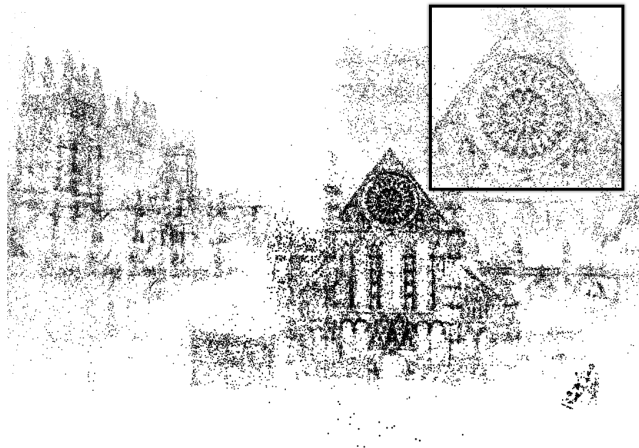
If at least two point correspondences are given, a homogeneous linear system of equations is obtained. The optimal solution, in the LSQ sense, is given via calculating the null-vector of the coefficient matrix.

### 6.3. Trajectories of Fast-moving Objects

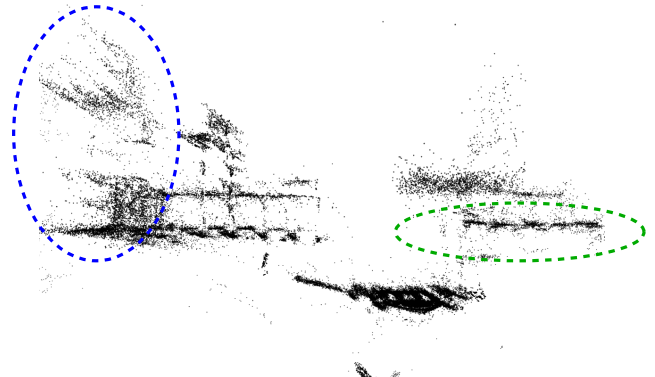
We show additional visualizations of trajectory estimation of fast-moving objects in Fig. 9. After extracting blur kernels that encode the object motion, we apply multiple line segment fitting. The estimated line segments are colored in red. The ground truth line segments are generated by applying a classical state-of-the-art object tracking algorithm on high-speed camera footage with manual annotations, which is shown in green. Qualitatively, we compare to the sequential RANSAC implementation from [30]. Additionally, we show final trajectories after filtering and refinement [30].

## References

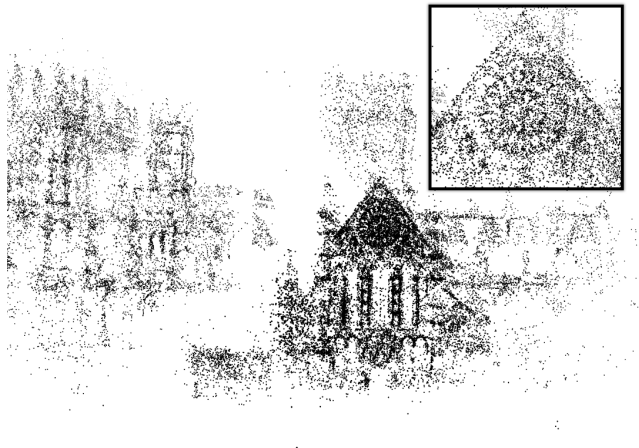
- [1] Paul Amayo, Pedro Piniés, Lina M Paz, and Paul Newman. Geometric multi-model fitting with a convex relaxation algorithm. In *Proc. Conf. on Computer Vision and Pattern Recognition*, pages 8138–8146, 2018.



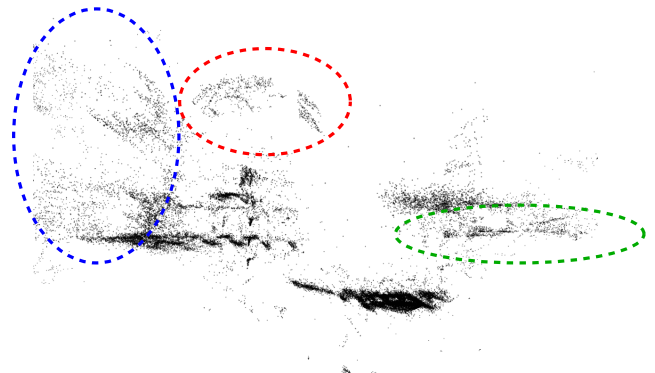
(a) Frontal view –  $\mathbf{E}$  + mult.  $\mathbf{H}_s$  (CC).



(b) Top-down view –  $\mathbf{E}$  + mult.  $\mathbf{H}_s$  (CC).



(c) Frontal view –  $\mathbf{E}$  matrices only.

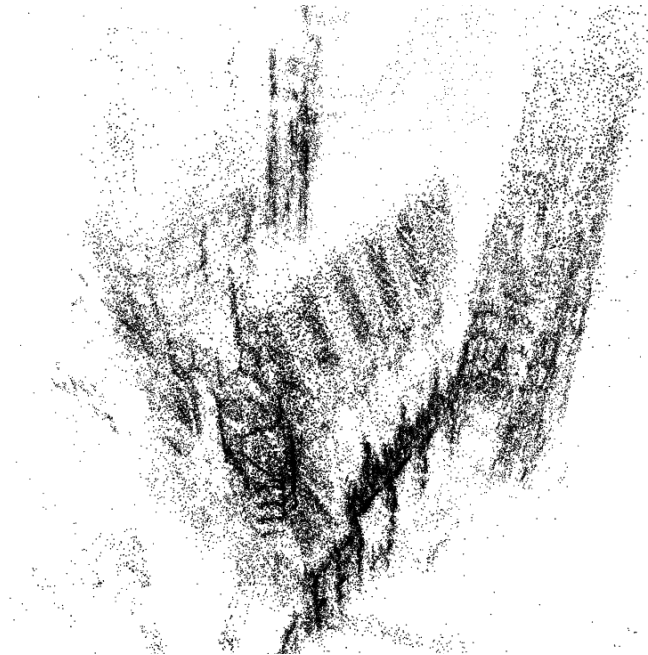


(d) Top-down view –  $\mathbf{E}$  matrices only.

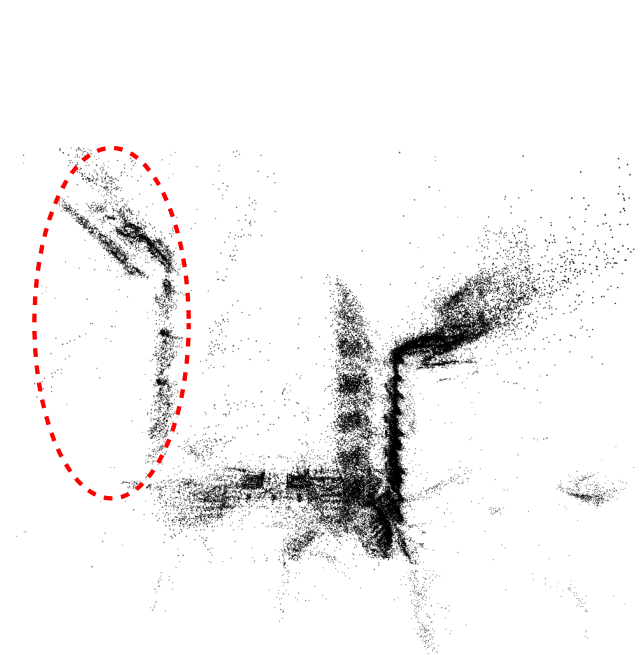
Figure 7: Visual comparison of the reconstructions of Yorkminster by [55] when initialized by the proposed ( $\mathbf{E}$  + mult.  $\mathbf{H}_s$  (CC); top row) and traditional ( $\mathbf{E}$  matrices; bottom) techniques. Blue and green ellipses highlight areas that the proposed algorithm reconstructs significantly more accurately than the traditional approach. The red ellipse points to an erroneous area. “CC” stands for using the proposed sampler in Progressive- $\mathbf{X}^+$  for multi-homography fitting.

- [2] Daniel Barath, Maksym Ivashechkin, and Jiri Matas. Progressive NAPSAC: sampling from gradually growing neighborhoods. *arXiv preprint arXiv:1906.02295*, 2019.
- [3] Daniel Barath and Jiri Matas. Graph-cut RANSAC. *Proc. Conf. on Computer Vision and Pattern Recognition*, 2018.
- [4] Daniel Barath and Jiri Matas. Multi-class model fitting by energy minimization and mode-seeking. In *Proc. European Conf. on Computer Vision*, 2018.
- [5] Daniel Barath and Jiri Matas. Progressive-X: Efficient, anytime, multi-model fitting algorithm. In *Proc. Int. Conf. on Computer Vision*, pages 3780–3788, 2019.
- [6] Daniel Barath, Dmytro Mishkin, Ivan Eichhardt, Ilia Shipachev, and Jiri Matas. Efficient initial pose-graph generation for Global SfM. In *Proc. Conf. on Computer Vision and Pattern Recognition*, 2021.
- [7] Daniel Barath, Jana Noskova, Maksym Ivashechkin, and Jiri Matas. MAGSAC++, a fast, reliable and accurate robust estimator. In *Proc. Conf. on Computer Vision and Pattern Recognition*, pages 1304–1312, 2020.
- [8] Snehal Bhayani, Torsten Sattler, Daniel Barath, Patrik Beliansky, Janne Heikkila, and Zuzana Kukelova. Calibrated and partially calibrated semi-generalized homographies, 2021.
- [9] Yuri Boykov and Vladimir Kolmogorov. An experimental comparison of min-cut/max-flow algorithms for energy minimization in vision. *IEEE Trans. Pattern Analysis and Machine Intelligence*, 2004.
- [10] A. Z. Broder. On the resemblance and containment of documents. In *Compression and complexity of sequences 1997. proceedings*, pages 21–29. IEEE, 1997.

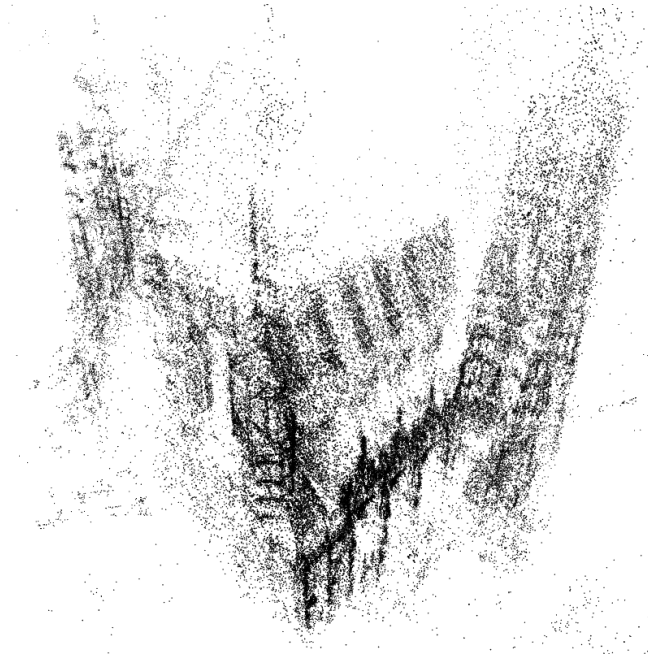




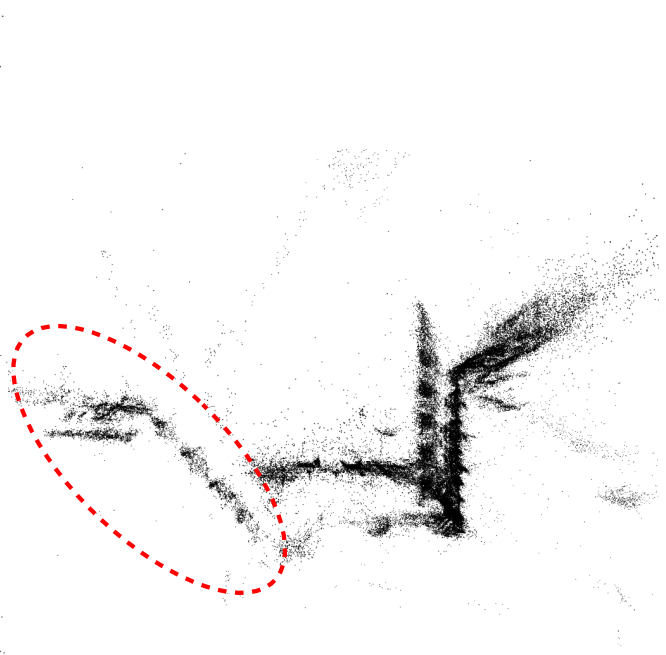
(a) Frontal view –  $\mathbf{E}$  + mult.  $\mathbf{H}_s$  (CC).



(b) Top-down view –  $\mathbf{E}$  + mult.  $\mathbf{H}_s$  (CC).



(c) Frontal view –  $\mathbf{E}$  matrices only.



(d) Top-down view –  $\mathbf{E}$  matrices only.

Figure 8: Visual comparison of the reconstructions of Vienna Cathedral by [55] when initialized by the proposed ( $\mathbf{E}$  + mult.  $\mathbf{H}_s$  (CC); top) and traditional ( $\mathbf{E}$  matrices; bottom) techniques. The proposed approach preserves the parallelism of the walls of the cathedral (red ellipse). “CC” stands for using the proposed sampler in Progressive- $X^+$  for multi-homography fitting.

[11] Avishek Chatterjee and Venu Madhav Govindu. Efficient and robust large-scale rotation averaging. In *Proc. Int. Conf. on Computer Vision*, pages 521–528, 2013.

[12] Ondrej Chum and Jiri Matas. Matching with PROSAC-

progressive sample consensus. In *Proc. Conf. on Computer Vision and Pattern Recognition*. IEEE, 2005.

[13] O. Chum, T. Werner, and J. Matas. Epipolar geometry estimation via RANSAC benefits from the oriented epipolar

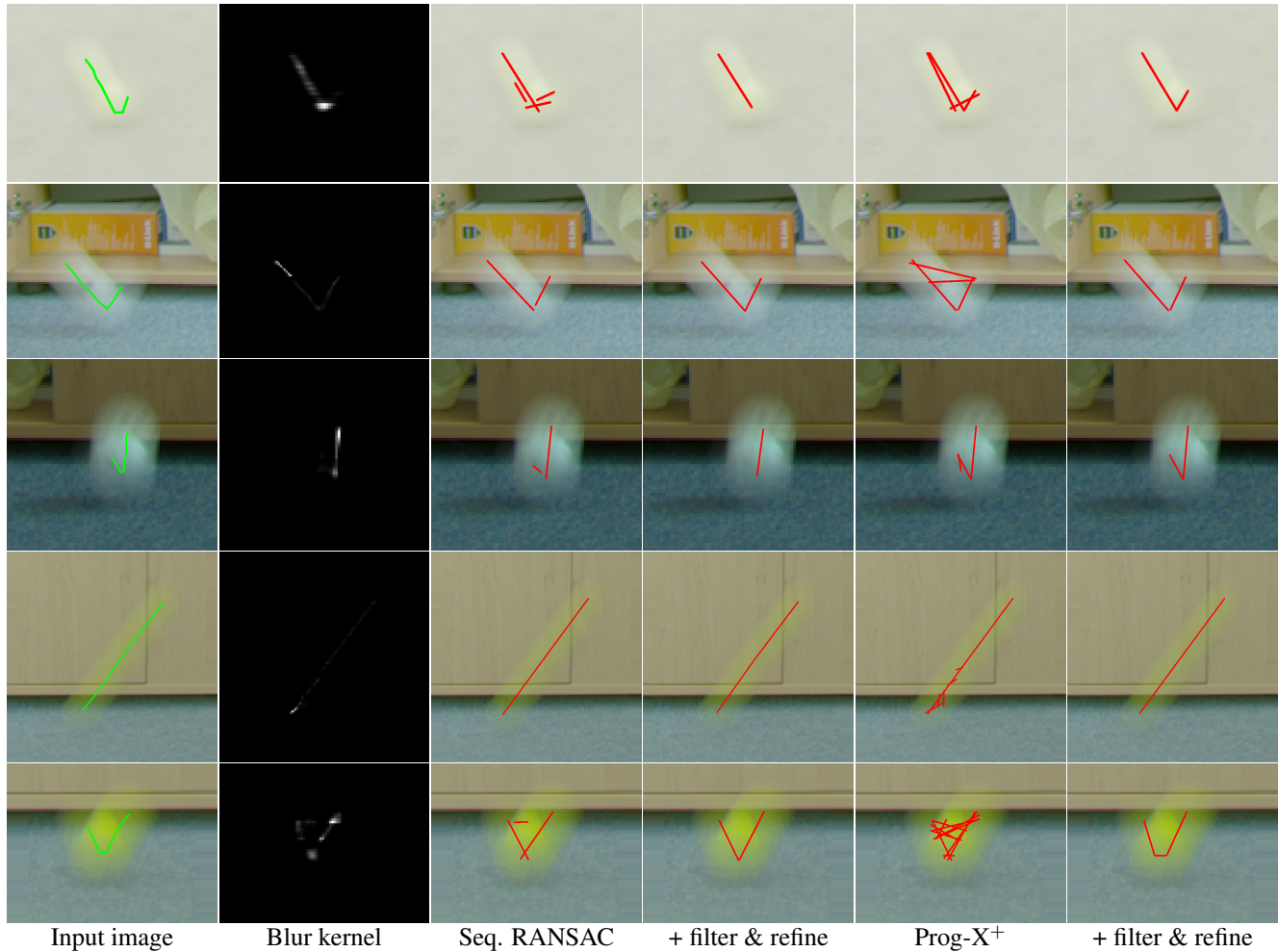


Figure 9: Fitting multiple line segments for trajectory estimation of fast-moving objects. The estimated and ground truth line segments are colored by red and green, respectively. The original Tracking by Deblatting [30] method for trajectory estimation of fast-moving objects uses the sequential RANSAC algorithm. Therefore, we report results using their implementation. The filtering and refinement are done by the method proposed in [30]. After post-processing by filtering and refinement, the results from Progressive- $X^+$  more often cover the sought trajectory than by the other methods. The results of seq. RANSAC, besides being qualitatively worse, *i.e.* missing a segment in rows 1, 3, and 5, suffer from the single-model assignment of inliers which shows as a gap between consecutive segments. The width of the gap equals to the inlier threshold of seq. RANSAC.

- constraint. In *Proc. Int. Conf. on Pattern Recognition*, 2004.
- [14] Ondrej Chum, Tomas Werner, and Jiri Matas. Two-view geometry estimation unaffected by a dominant plane. In *Proc. Conf. on Computer Vision and Pattern Recognition*. IEEE, 2005.
- [15] Dorin Comaniciu and Peter Meer. Mean shift analysis and applications. In *Proc. Int. Conf. on Computer Vision*, volume 2, pages 1197–1203. IEEE, 1999.
- [16] Andrew Delong, Lena Gorelick, Olga Veksler, and Yuri Boykov. Minimizing energies with hierarchical costs. *Int. Journal of Computer Vision*, 2012.
- [17] Martin Ester, Hans-Peter Kriegel, Jörg Sander, Xiaowei Xu, et al. A density-based algorithm for discovering clusters in large spatial databases with noise. In *Kdd*, volume 96, pages 226–231, 1996.
- [18] Martin A. Fischler and Robert C. Bolles. Random sample consensus: a paradigm for model fitting with applications to image analysis and automated cartography. *Communications of the ACM*, 1981.
- [19] Andreas Geiger, Philip Lenz, and Raquel Urtasun. Are we ready for autonomous driving? the KITTI vision benchmark suite. In *Proc. Conf. on Computer Vision and Pattern Recognition*, 2012.
- [20] Nicolas Guil and Emilio L. Zapata. Lower order circle and ellipse Hough transform. *Pattern Recognition*, 1997.
- [21] Richard Hartley. In defense of the eight-point algorithm.

- IEEE Trans. Pattern Analysis and Machine Intelligence*, 1997.
- [22] Richard Hartley and Andrew Zisserman. *Multiple view geometry in computer vision*. Cambridge University Press, 2003.
  - [23] Kaiming He, Xiangyu Zhang, Shaoqing Ren, and Jian Sun. Deep residual learning for image recognition. In *Proc. Conf. on Computer Vision and Pattern Recognition*, 2016.
  - [24] P. V. C. Hough. Method and means for recognizing complex patterns, 1962.
  - [25] John Illingworth and Josef Kittler. A survey of the Hough transform. *Computer Vision, Graphics, and Image Processing*, 1988.
  - [26] Hossam Isack and Yuri Boykov. Energy-based geometric multi-model fitting. *Int. Journal of Computer Vision*, 2012.
  - [27] Yasushi Kanazawa and Hiroshi Kawakami. Detection of planar regions with uncalibrated stereo using distributions of feature points. In *Proc. British Machine Vision Conf.*, 2004.
  - [28] Florian Kluger, Eric Brachmann, Hanno Ackermann, Carsten Rother, Michael Ying Yang, and Bodo Rosenhahn. CONSAC: Robust multi-model fitting by conditional sample consensus. In *Proc. Conf. on Computer Vision and Pattern Recognition*, pages 4634–4643, 2020.
  - [29] Jan Kotera, Jiri Matas, and Filip Šroubek. Restoration of fast moving objects. *IEEE Trans. Image Processing*, 29:8577–8589, 2020.
  - [30] Jan Kotera, Denys Rozumnyi, Filip Šroubek, and Jiri Matas. Intra-frame object tracking by deblatting. In *International Conference on Computer Vision Workshops*, Oct 2019.
  - [31] Jan Kotera and Filip Šroubek. Motion estimation and deblurring of fast moving objects. In *Proc. Int. Conf. on Image Processing*, pages 2860–2864, Oct 2018.
  - [32] Alan H Lipkus. A proof of the triangle inequality for the Tanimoto distance. *Journal of Mathematical Chemistry*, 26(1):263–265, 1999.
  - [33] Jiayi Ma, Xingyu Jiang, Aoxiang Fan, Junjun Jiang, and Junchi Yan. Image matching from handcrafted to deep features: A survey. *Int. Journal of Computer Vision*, 129(1):23–79, 2021.
  - [34] Luca Magri and Andrea Fusiello. T-Linkage: A continuous relaxation of J-Linkage for multi-model fitting. In *Proc. Conf. on Computer Vision and Pattern Recognition*, 2014.
  - [35] Luca Magri and Andrea Fusiello. Robust multiple model fitting with preference analysis and low-rank approximation. In *Proc. British Machine Vision Conf.*, 2015.
  - [36] Luca Magri and Andrea Fusiello. Multiple model fitting as a set coverage problem. In *Proc. Conf. on Computer Vision and Pattern Recognition*, 2016.
  - [37] Ezio Malis and Manuel Vargas. *Deeper understanding of the homography decomposition for vision-based control*. PhD thesis, INRIA, 2007.
  - [38] Jiri Matas, Csaba Galambos, and Josef Kittler. Robust detection of lines using the progressive probabilistic Hough transform. *Computer Vision and Image Understanding*, 2000.
  - [39] D. R. Myatt, Philip Torr, Slawomir J. Nasuto, Mark J. Bishop, and R. Craddock. NAPSAC: High noise, high dimensional robust estimation - it’s in the bag. In *Proc. British Machine Vision Conf.*, 2002.
  - [40] Hyeonwoo Noh, Andre Araujo, Jack Sim, Tobias Weyand, and Bohyung Han. Large-scale image retrieval with attentive deep local features. In *Proc. Conf. on Computer Vision and Pattern Recognition*, pages 3456–3465, 2017.
  - [41] Trung Thanh Pham, Tat-Jun Chin, Konrad Schindler, and David Suter. Interacting geometric priors for robust multi-model fitting. *IEEE Trans. Image Processing*, 2014.
  - [42] Filip Radenović, Giorgos Tolias, and Ondrej Chum. Fine-tuning CNN image retrieval with no human annotation. *IEEE Trans. Pattern Analysis and Machine Intelligence*, 2018.
  - [43] R. Raguram, O. Chum, M. Pollefeys, J. Matas, and J.-M. Frahm. USAC: a universal framework for random sample consensus. *IEEE Trans. Pattern Analysis and Machine Intelligence*, 2013.
  - [44] R Tyrrell Rockafellar and Roger J-B Wets. *Variational analysis*, volume 317. Springer Science & Business Media, 2009.
  - [45] Paul L. Rosin. Ellipse fitting by accumulating five-point fits. *Pattern Recognition Letters*, 1993.
  - [46] Denys Rozumnyi, Jan Kotera, Filip Šroubek, and Jiri Matas. Non-causal tracking by deblatting. In Gernot A. Fink, Simone Frintrop, and Xiaoyi Jiang, editors, *German Conference on Pattern Recognition*, pages 122–135, Cham, 2019. Springer International Publishing.
  - [47] Denys Rozumnyi, Jan Kotera, Filip Šroubek, Lukas Novotný, and Jiri Matas. The world of fast moving objects. In *Proc. Conf. on Computer Vision and Pattern Recognition*, pages 4838–4846, July 2017.
  - [48] Denys Rozumnyi, Jan Kotera, Filip Šroubek, and Jiri Matas. Sub-frame appearance and 6D pose estimation of fast moving objects. In *Proc. Conf. on Computer Vision and Pattern Recognition*, pages 6777–6785, 2020.
  - [49] Denys Rozumnyi, Jiri Matas, Filip Šroubek, Marc Pollefeys, and Martin R. Oswald. FMODETECT: Robust detection and trajectory estimation of fast moving objects, 2020.
  - [50] Denys Rozumnyi, Martin R. Oswald, Vittorio Ferrari, Jiri Matas, and Marc Pollefeys. DeFMO: Deblurring and shape recovery of fast moving objects, 2020.
  - [51] Johannes L Schonberger and Jan-Michael Frahm. Structure-from-motion revisited. In *Proc. Conf. on Computer Vision and Pattern Recognition*, pages 4104–4113, 2016.
  - [52] Erich Schubert, Jörg Sander, Martin Ester, Hans Peter Kriegel, and Xiaowei Xu. DBSCAN revisited, revisited: why and how you should (still) use DBSCAN. *ACM Transactions on Database Systems*, 42(3):1–21, 2017.
  - [53] Noah Snavely, Steven M Seitz, and Richard Szeliski. Photo tourism: exploring photo collections in 3D. In *ACM siggraph*, pages 835–846. 2006.
  - [54] H. Stewenius, C. Engels, and D. Nistér. Recent developments on direct relative orientation. *Journal of Photogrammetry and Remote Sensing*, 60(4):284–294, 2006.
  - [55] Christopher Sweeney, Tobias Hollerer, and Matthew Turk. Theia: A fast and scalable structure-from-motion library. In *Proceedings of the 23rd ACM international conference on Multimedia*, pages 693–696, 2015.
  - [56] T. T. Tanimoto. Elementary mathematical theory of classification and prediction. 1958.



- [57] Roberto Toldo and Andrea Fusiello. Robust multiple structures estimation with J-Linkage. In *Proc. European Conf. on Computer Vision*, 2008.
- [58] Roberto Tron and Rene Vidal. A benchmark for the comparison of 3-d motion segmentation algorithms. In *Proc. Conf. on Computer Vision and Pattern Recognition*, 2007.
- [59] E. Vincent and Robert Laganière. Detecting planar homographies in an image pair. In *International Symposium on Image and Signal Processing and Analysis*, 2001.
- [60] Filip Šroubek and Jan Kotera. Motion blur prior. In *Proc. Int. Conf. on Image Processing*, pages 928–932, 2020.
- [61] Hanzi Wang, Guobao Xiao, Yan Yan, and David Suter. Mode-seeking on hypergraphs for robust geometric model fitting. In *Proc. Int. Conf. on Computer Vision*, 2015.
- [62] Hanzi Wang, Guobao Xiao, Yan Yan, and David Suter. Searching for representative modes on hypergraphs for robust geometric model fitting. *IEEE Trans. Pattern Analysis and Machine Intelligence*, 2018.
- [63] Kyle Wilson and Noah Snavely. Robust global translations with 1DSfM. In *Proc. European Conf. on Computer Vision*, 2014.
- [64] Kyle Wilson and Noah Snavely. Robust global translations with 1DSfM. In *Proc. European Conf. on Computer Vision*, pages 61–75. Springer, 2014.
- [65] Hoi Sim Wong, Tat-Jun Chin, Jin Yu, and David Suter. Dynamic and hierarchical multi-structure geometric model fitting. In *Proc. Int. Conf. on Computer Vision*, 2011.
- [66] Lei Xu, Erkki Oja, and Pekka Kultanen. A new curve detection method: randomized Hough transform (rht). *Pattern Recognition Letters*, 1990.
- [67] Wei Zhang and Jana Kosecká. Nonparametric estimation of multiple structures with outliers. In *Dynamical Vision*. Springer, 2007.
- [68] Qing Zhao, Yun Zhang, Qianqing Qin, and Bin Luo. Quantized residual preference based linkage clustering for model selection and inlier segmentation in geometric multi-model fitting. *Sensors*, 20(13):3806, 2020.
- [69] Enliang Zheng and Changchang Wu. Structure from motion using structure-less resection. In *Proc. Int. Conf. on Computer Vision*, pages 2075–2083, 2015.
- [70] Marco Zuliani, C. S. Kenney, and Bangalore Manjunath. The multiRANSAC algorithm and its application to detect planar homographies. In *Proc. Int. Conf. on Image Processing*. IEEE, 2005.

Table 6: The results of the global SfM algorithm from [55] on the scenes from the 1DSfM dataset [63] when initialized by the pose-graph estimated from essential matrices (**E** matrix), and the proposed Progressive- $X^+$  combined either with Progressive NAPSAC [2] or the proposed Connected Components (CC) samplers. As ground truth, we used reconstructions from COLMAP [51]. The averages and average medians of the rotation and position errors are reported in Table 5.

	# views	# tracks	orientation err ( $^{\circ}$ )			position err (m)			focal len. err ( $\times 10^{-2}$ )		
			AVG	MED	STD	AVG	MED	STD	AVG	MED	STD
Alamo											
<b>E</b> matrix	493	104 894	<b>2.46</b>	<b>0.59</b>	3.76	<b>1.60</b>	<b>1.36</b>	<b>3.98</b>	<b>0.02</b>	<b>0.01</b>	<b>0.05</b>
<b>E</b> + mult. <b>Hs</b>	<b>495</b>	<b>110 243</b>	2.80	0.81	3.91	1.79	1.88	4.73	<b>0.02</b>	<b>0.01</b>	<b>0.05</b>
<b>E</b> + mult. <b>Hs</b> (CC)	494	105 920	2.59	0.62	<b>3.63</b>	1.68	1.58	4.19	<b>0.02</b>	<b>0.01</b>	<b>0.05</b>
Ellis Island											
<b>E</b> matrix	211	<b>31 200</b>	4.21	2.90	4.69	5.59	3.43	10.57	<b>0.02</b>	<b>0.01</b>	<b>0.02</b>
<b>E</b> + mult. <b>Hs</b>	210	30 610	<b>3.49</b>	<b>2.33</b>	<b>3.00</b>	<b>4.27</b>	<b>3.09</b>	<b>8.22</b>	<b>0.02</b>	<b>0.01</b>	<b>0.02</b>
<b>E</b> + mult. <b>Hs</b> (CC)	<b>215</b>	31 182	4.61	2.61	3.87	5.86	3.89	11.59	<b>0.02</b>	<b>0.01</b>	<b>0.02</b>
Madrid Metropolis											
<b>E</b> matrix	299	56 102	11.38	0.69	14.50	1.09	8.06	1.36	<b>0.06</b>	<b>0.03</b>	<b>0.10</b>
<b>E</b> + mult. <b>Hs</b>	<b>327</b>	50 438	<b>4.00</b>	<b>0.30</b>	<b>5.63</b>	<b>0.60</b>	<b>2.86</b>	<b>0.90</b>	0.07	<b>0.03</b>	0.14
<b>E</b> + mult. <b>Hs</b> (CC)	298	<b>57 457</b>	8.06	0.58	12.11	1.00	4.77	1.18	<b>0.06</b>	<b>0.03</b>	<b>0.10</b>
Montreal Notre Dame											
<b>E</b> matrix	432	106 101	<b>1.34</b>	<b>0.41</b>	8.64	<b>0.82</b>	<b>0.38</b>	<b>1.22</b>	<b>0.02</b>	<b>0.01</b>	<b>0.03</b>
<b>E</b> + mult. <b>Hs</b>	435	<b>106 498</b>	1.52	0.46	<b>7.84</b>	0.89	0.47	1.31	<b>0.02</b>	<b>0.01</b>	<b>0.03</b>
<b>E</b> + mult. <b>Hs</b> (CC)	<b>436</b>	104 802	1.45	0.46	8.03	0.97	0.45	1.61	<b>0.02</b>	<b>0.01</b>	<b>0.03</b>
NYC Library											
<b>E</b> matrix	270	<b>57 235</b>	53.59	14.08	<b>3.86</b>	14.10	52.95	7.26	<b>0.03</b>	<b>0.01</b>	<b>0.04</b>
<b>E</b> + mult. <b>Hs</b>	<b>271</b>	56 435	<b>5.20</b>	<b>2.94</b>	3.96	<b>4.97</b>	<b>4.23</b>	6.73	<b>0.03</b>	<b>0.01</b>	<b>0.04</b>
<b>E</b> + mult. <b>Hs</b> (CC)	270	55 418	6.44	3.11	4.26	5.04	5.54	<b>6.59</b>	<b>0.03</b>	<b>0.01</b>	<b>0.04</b>
Piazza del Popolo											
<b>E</b> matrix	<b>291</b>	42 823	7.24	3.82	3.33	4.91	7.61	4.34	<b>0.03</b>	<b>0.02</b>	<b>0.04</b>
<b>E</b> + mult. <b>Hs</b>	288	<b>44 457</b>	6.99	3.32	3.26	4.16	7.51	4.19	<b>0.03</b>	<b>0.02</b>	0.05
<b>E</b> + mult. <b>Hs</b> (CC)	<b>291</b>	43 510	<b>5.37</b>	<b>2.53</b>	<b>1.46</b>	<b>3.28</b>	<b>5.46</b>	<b>3.54</b>	<b>0.03</b>	<b>0.02</b>	<b>0.04</b>
Piccadilly											
<b>E</b> matrix	<b>1869</b>	210 821	<b>4.71</b>	0.35	<b>13.53</b>	0.70	2.00	<b>1.05</b>	<b>0.05</b>	<b>0.03</b>	0.15
<b>E</b> + mult. <b>Hs</b>	1656	141 661	10.15	0.48	24.75	0.87	2.55	1.11	<b>0.05</b>	<b>0.03</b>	<b>0.14</b>
<b>E</b> + mult. <b>Hs</b> (CC)	1860	<b>220 045</b>	4.96	<b>0.31</b>	14.83	<b>0.66</b>	<b>1.68</b>	<b>1.05</b>	<b>0.05</b>	<b>0.03</b>	0.15
Roman Forum											
<b>E</b> matrix	989	<b>208 457</b>	4.87	<b>14.76</b>	4.68	<b>22.25</b>	3.86	82.77	<b>0.03</b>	<b>0.02</b>	<b>0.07</b>
<b>E</b> + mult. <b>Hs</b>	991	204 432	<b>4.56</b>	15.64	<b>3.37</b>	22.90	<b>3.78</b>	82.49	<b>0.03</b>	<b>0.02</b>	<b>0.07</b>
<b>E</b> + mult. <b>Hs</b> (CC)	<b>995</b>	206 641	4.85	15.78	3.59	23.61	4.01	<b>82.29</b>	<b>0.03</b>	<b>0.02</b>	<b>0.07</b>
Tower of London											
<b>E</b> matrix	<b>406</b>	<b>96 481</b>	6.03	<b>9.48</b>	12.55	<b>25.04</b>	<b>2.42</b>	<b>38.79</b>	<b>0.02</b>	<b>0.01</b>	<b>0.03</b>
<b>E</b> + mult. <b>Hs</b>	397	95 394	<b>5.29</b>	10.58	<b>6.29</b>	26.47	3.39	40.70	<b>0.02</b>	<b>0.01</b>	<b>0.03</b>
<b>E</b> + mult. <b>Hs</b> (CC)	405	96 088	5.83	10.94	8.87	26.56	3.54	40.54	<b>0.02</b>	<b>0.01</b>	<b>0.03</b>
Trafalgar											
<b>E</b> matrix	<b>4111</b>	<b>354 494</b>	18.03	16.79	32.09	23.92	10.70	<b>29.63</b>	<b>0.02</b>	<b>0.01</b>	<b>0.03</b>
<b>E</b> + mult. <b>Hs</b>	4097	349 621	19.10	<b>16.14</b>	41.86	<b>23.74</b>	<b>7.20</b>	30.73	<b>0.02</b>	<b>0.01</b>	<b>0.03</b>
<b>E</b> + mult. <b>Hs</b> (CC)	4088	349 784	<b>18.00</b>	17.09	<b>31.97</b>	24.79	10.93	30.64	<b>0.02</b>	<b>0.01</b>	<b>0.03</b>
Vienna Cathedral											
<b>E</b> matrix	705	160 363	14.47	7.49	9.86	10.96	9.40	11.55	<b>0.02</b>	<b>0.01</b>	<b>0.05</b>
<b>E</b> + mult. <b>Hs</b>	612	92 051	26.35	13.79	29.71	22.85	13.10	25.45	<b>0.02</b>	<b>0.01</b>	<b>0.05</b>
<b>E</b> + mult. <b>Hs</b> (CC)	<b>707</b>	<b>160 503</b>	<b>4.72</b>	<b>6.97</b>	<b>4.84</b>	<b>10.15</b>	<b>3.18</b>	<b>11.03</b>	<b>0.02</b>	<b>0.01</b>	<b>0.05</b>
Yorkminster											
<b>E</b> matrix	399	98 396	5.52	7.61	3.57	12.13	4.99	17.70	<b>0.03</b>	<b>0.01</b>	<b>0.04</b>
<b>E</b> + mult. <b>Hs</b>	<b>402</b>	100 985	5.68	7.74	3.46	12.68	5.11	20.03	<b>0.03</b>	<b>0.01</b>	<b>0.04</b>
<b>E</b> + mult. <b>Hs</b> (CC)	399	<b>109 132</b>	<b>3.49</b>	<b>6.27</b>	<b>2.90</b>	<b>11.26</b>	<b>2.91</b>	<b>17.12</b>	<b>0.03</b>	<b>0.01</b>	<b>0.04</b>